Journal of
Materials Chemistry A

PAPER

View Article Online
View Journal | View Issue

Cite this: J. Mater. Chem. A, 2019, 7, 22604

Influence of bromide content on iodide migration in inverted $MAPb(I_{1-x}Br_x)_3$ perovskite solar cells†

Rodrigo García-Rodríguez, *[a] Dominic Ferdani,[a] Samuel Pering,[a] Peter J. Baker [b] and Petra J. Cameron *[a]

Received 13th August 2019
Accepted 19th September 2019

DOI: 10.1039/c9ta08848b

rsc.li/materials-a

The effect of a systematic increase in the bromide content on mixed anion methyl ammonium lead halide, $MAPb(I_{1-x}Br_x)_3$, perovskite solar cells is investigated. We show that at a critical bromide concentration (7.5%) we supress the slow impedance response from the cells. We link the changing impedance spectrum to a large increase in the activation energy for iodide motion. These results are corroborated by muon spin relaxation measurements, where we show that at the concentration of bromide typically used in high performance perovskite solar cells (17%) there is no sign of iodide motion in powders. Finally, we show *JV* curve hysteresis as a function of bromide content. The scan rate at which the maximum hysteresis index is observed does not change as the % Br is increased, leading us to conclude that the low frequency impedance response and the *JV* curve hysteresis are not caused by the same mobile ions.

Introduction

Research into perovskite solar cells (PSC) has been a focus of the photovoltaic community over the last 10 years, mainly as no other photovoltaic technology has observed a more pronounced rise in the efficiency of devices. PSC have increased from an efficiency of 3.8% in 2009 (ref. 1) to a certified efficiency of 20.9% for a 1 cm^2 cell[2,3] and recently to 24.2% for an aperture area of 0.096 cm^2.[4] The steep rise in efficiency is partly a consequence of lessons learned during the development of other emerging photovoltaics technologies such as thin film solar cells,[5,6] organic solar cells[7] and dye-sensitized solar cells.[8,9] Due to the ionic nature of the components, perovskite materials are fairly easy to synthesize *via* solution-based methods[10–13] and at the same time, the performance of PSC has proven to be very resilient to defects.[14,15] It is also possible to change the chemical composition of the lead halide perovskites to effectively and systematically tune their bandgap,[16–18] making them particularly attractive for a wide variety of applications including light emitting diodes[16,19,20] and tandem solar cells.[21,22] However, in spite of these promising features, the development of perovskite solar cells still presents important challenges: low stability, particularly under high humidity conditions,[23–25] and a hysteretic behavior that appears to be intrinsic to lead halide perovskite devices.[12,13,26–28] Stability and hysteresis have been closely linked to the ionic nature of the perovskites. Several studies have shown that a very small activation energy has to be overcome for the iodide anion (0.2–0.7 eV) and methyl ammonium cation (MA^+) (0.5–0.8 eV) to move through the perovskite structure.[11–13,29–33] The consensus is that the activation barrier to iodide and methyl ammonium motion is low enough to contribute to the low stability of the perovskite devices.[11–15,28,29,31,32] Hysteretic behavior has been related to ion migration and the redistribution of charge inside the perovskite film following the application of an electrical potential.[11,12] Experimental evidence of ion migration has been found by employing photo-thermal induced resonance microscopy,[34] by polarizing the perovskite structure (also known as poling) and then employing complementary techniques such as X-ray diffraction (XRD) to analyze the chemical composition of the perovskite after poling,[28,30,35] and *via* temperature-dependent impedance spectroscopy[31,33] and current–potential curves.[11,13,32] The activation energies obtained from these characterization techniques are in the range of the values predicted theoretically.

It has been proposed that ion motion can be altered by changing the chemical composition of the perovskite. In a theoretical study, Lin *et al.*[36] found that the presence of bromide in methylammonium lead iodide increased ion diffusion barriers and hindered the movement of ions in the perovskite due to a more compact crystal structure. By substituting iodide ions with the smaller bromide ions, Noh *et al.*[37] and Ruess *et al.*[38] managed to increase the stability of the perovskite under high humidity conditions. The increase in stability was also attributed to a more compact structure. High bromide concentrations (>20%) are difficult to study as phase separation into iodide and bromide rich regions occurs under illumination.[38–41] Yoon *et al.*[39] proposed that anion segregation

---

[a] Department of Chemistry, University of Bath, Bath BA27AY, UK. E-mail: rgr25@bath.ac.uk; p.j.cameron@bath.ac.uk

[b] ISIS Pulsed Neutron and Muon Source, Rutherford Appleton Laboratory, Harwell Oxford, Didcot OX110QX, UK

† Electronic supplementary information (ESI) available. See DOI: 10.1039/c9ta08848b

is highly influenced by the concentration of defect sites, and found that a stoichiometric excess of the halides in the perovskite composition may help to reduce phase separation. Hysteresis can also be modified by changing the configuration of the devices.[28,42–44] Although changes to the perovskite structure have been shown to strongly influence material stability and *I–V* curve hysteresis, a systematic experimental study on the influence of anion mixing on iodide migration in perovskite cells has not been reported.

Here we study the influence of anion ratios on methyl ammonium lead halide devices by gradually increasing the bromide concentration in inverted $MAPbI_3$ perovskite solar cells. We use impedance spectroscopy measurements at different temperatures to relate the bromide concentration to the activation energy for iodide migration within the material. We show that iodide motion is strongly suppressed at low concentrations of bromide. Our impedance results are corroborated by muon spin relaxation measurements which show that for the mixed halide perovskite $MAPb(I_{0.83}Br_{0.17})_3$, no iodide diffusion is observed. By measuring current–voltage curves at different scan rates, we analyze the influence of bromide content on the hysteretic behavior and determine the scan rate at which the hysteresis is highest. We then compare the information on ion motion obtained from hysteresis and impedance measurements, highlighting fundamental differences between both characterization techniques.

Experimental

All chemicals were purchased from Sigma-Aldrich unless otherwise noted. [6,6]-Phenyl-C61-butyric acid methyl ester (PCBM) was purchased from Ossila (Sheffield, United Kingdom).

Perovskite solar cells with inverted configuration

Substrate preparation. TEC-15 fluorine doped tin oxide (FTO) glass (Sigma Aldrich) was used as substrate. A strip of the FTO glass where the metallic contact of the anode will be located was chemically etched and removed with a 2 M solution of hydrochloric acid (HCl) and zinc powder. The FTO was rinsed with deionized water and sequentially sonicated for 15 minutes at 50 °C with 2% Hellmanex detergent, water, acetone, ethanol and isopropanol. The FTO was dried with air and prior to the deposition of the nickel oxide layer it was placed under ozone lamp irradiation for 30 min (UV/Ozone ProCleaner, Bioforce Nanosciences).

Hole-selective contact. A 0.2 M solution of nickel acetate tetrahydrate in 2-methoxy ethanol was prepared. Once the nickel acetate was completely dissolved, a small amount of ethanolamine was dropped into the solution (12 μL of ethanolamine per mL of the nickel acetate solution). When the solution was completely homogeneous, it was filtered through a PTFE syringe filter (45 μm). 100 μL of the solution was spread over an FTO substrate and spin coated at 3000 rpm for 30 seconds. A strip of the NiO layer was removed with 2-methoxy ethanol, where the metallic contact of the cathode will be deposited. The FTO was then placed on a hot plate at 500 °C for 30 minutes.

Perovskite layer. A 1.25 M solution of lead iodide (PbI_2) and methyl ammonium iodide (MAI) in a 4 : 1 v/v mixture of dimethyl formamide (DMF)/dimethyl sulfoxide (DMSO) was prepared. The solution was stirred until the chemicals were completely dissolved. For the cells with different bromide content, a 1.25 M solution of lead bromide ($PbBr_2$) and methyl ammonium bromide (MABr) in a 4 : 1 v/v mixture of DMF/DMSO was prepared. Depending on the bromide concentration required, the corresponding ratios of $MAPbI_3$ and the $MAPbBr_3$ were mixed. The solution was stirred for 30 minutes to homogenize and was filtered through a PTFE syringe filter (45 μm).

Electron-selective contact. A 22 mM solution of PCBM in chlorobenzene was prepared. The solution was heated at 60 °C and stirred for 30 minutes to ensure proper dissolution. The solution was then filtered through a PTFE syringe filter (45 μm). A 1.4 mM solution of bathocuproine (BCP) in ethanol was also prepared.

Solar cells assembly. Perovskite deposition was done inside a glove box with nitrogen atmosphere. The perovskite solution was spread over the NiO layer and spin coated at 4000 rpm for 30 seconds. 200 μL of ethyl acetate was dropped over the perovskite film 7 seconds after the beginning of the spin coating. The perovskite film was then placed on a hot plate at 100 °C for 10 minutes. After the perovskite had cooled down, the PCBM solution was spread over the surface of the perovskite and spin coated at 3000 rpm for 30 seconds and left to dry. Finally, the BCP solution is spread and spin coated over the PCBM layer at 6000 rpm for 30 seconds and let to dry. One strip of the perovskite cell was removed with a metallic blade where the metallic contact for the cathode will be deposited. The metallic contacts were deposited *via* silver evaporation in a high-vacuum physical vapour deposition chamber (Nano PVD, Moorfield nanotechnology, Cheshire, United Kingdom) with pressure below 1.5×10^{-5} mbar.

Optical characterization

UV-Vis transmittance and reflectance measurements were measured in a PerkinElmer Lambda 750 S UV/Vis Spectrometer, from 350 nm to 900 nm and with a step size of 1 nm. To account for internal reflections, the absorption of the material was calculated from the reflectance and transmission measurements according with $A \approx T/(1-R)^2$.[45] To calculate the bandgap of the material we employed Tauc plots for direct allowed transitions. To determine the chemical structure of the perovskite material, X-ray diffraction measurements were made with a STOE Transmission Diffractometer System STADI P, employing Cu-Kα radiation, scanning from 10° to 70° (2θ), with a 0.01 step size and an integration time of 20 seconds per point.

Current–voltage measurements

Current voltage curves of the solar cells were measured with a Keithley 2601A potentiostat under 1 sun illumination intensity provided by a single source, Class AAA solar simulator (T S

Space Systems LTS, Bucks, United Kingdom). The illumination intensity was calibrated with a certified WPVS monocrystalline silicon reference cell with a KG3 filter (Fraunhofer, ISE). 1.2 V was applied to each cell prior each measurement under illumination. A linear potential scan was applied from 1.2 V to 0 V and immediately from 0 V to 1.2 V at a scan rate of 100 mV s^{-1} with a step size of 10 mV. A mask of (0.25 × 0.25) cm^2 was employed to avoid additional contributions of scattered light in the glass. Each substrate accommodated 6 small solar cells.

Impedance spectroscopy measurements

Impedance spectroscopy and hysteresis measurements were performed with a ModuLab XM PhotoEchem system (Solartron Analytical). Before each measurement, the cell was under a 470 nm LED (Thorlabs M470L3) illumination (42.5 cm^{-2}) for 15 minutes to obtain a stable open circuit potential. The impedance measurements were made at open circuit potential under LED illumination and employing a small amplitude perturbation of 10 mV in the 100 kHz to 100 mHz frequency range. The electrochemical impedance spectrum was analyzed using Z-View software. The samples were mounted in a desiccator filled cell holder to prevent degradation. The temperature was controlled with a Peltier element and a Precision Peltier Temperature Controller TEC-1091 (Meerstetter Engineering, Rubigen, Switzerland).

Hysteresis measurements

A black mask with an aperture of (2.5 × 2.5) mm^2 was used to avoid additional contributions of scattered light to the sample. The cell was illuminated with a blue LED (Thorlabs 470 nm) at open circuit for 15 minutes or until the open circuit potential did not change over time. The illumination intensity employed was 4.4 mW cm^{-2}. 1.2 V was applied for 5 seconds prior to each scan. The cell was measured from open circuit conditions (V_{oc}) to short circuit conditions (J_{sc}) and immediately after from J_{sc} to V_{oc}. After each scan the cell was illuminated at open circuit potential for 2 minutes. The scan rates employed are presented in Table 1. The cell was measured from fast to slow scan rates.

Muon spectroscopy

Perovskite powders were prepared by a hot-casting method. To make a $MAPbBr_3$, a 1.9 M solution of MA and $PbBr_2$ in anhydrous DMF was prepared by stirring the precursors at 60 °C for one hour. The solution was subsequently cast onto a clean glass Petri dish at 110 °C and left for an hour to form a thick orange film. The film was scratched from the Petri dish to produce orange $MAPBr_3$ powder. The structure of the $MAPBr_3$ powder was confirmed by pXRD analysis. The synthesis procedure for the mixed halide perovskites was the same with the ratio of PbI_2 and $PbBr_2$ adjusted to give the desired stoichiometry.

Muon spin relaxation experiments were performed at the ISIS pulsed muon facility using the HIFI instrument. Approximately 1 g of sample was pressed into a metal sample holder forming a disc of approximately 1 mm thickness. The temperature was controlled between 40 and 410 K using a closed cycle refrigerator and hot stage. Measurements were taken at 4 different longitudinal fields at each temperature. Initial calibration of the instrument was performed by applying a 100 G transverse field. X-Ray diffraction patterns were obtained using a Bruker axs D8 advance powder X-ray diffractometer with Cu-Kα source and Ge monochromator.

Table 1 Scan rate and order of measurement for hysteresis analysis

#	Scan rate ($mV\ s^{-1}$)	#	Scan rate ($mV\ s^{-1}$)	#	Scan rate ($mV\ s^{-1}$)
1	7000	8	300	15	10
2	5000	9	200	16	7
3	3000	10	100	17	5
4	2000	11	70	18	3
5	1000	12	50	19	2
6	700	13	30	20	1
7	500	14	20	21	0.5

Results and discussion

$MAPb(I_{1-x}Br_x)_3$ films were prepared, where $x = 0$, 2.5%, 5%, 7.5%, 25% and 100%. The X-ray diffractograms for the films (Fig. 1) show the expected peaks associated with the (110) and (220) planes of a 3D perovskite structure.[38] As the amount of bromide increases, the peaks are displaced towards larger values of 2θ (the peak positions have been normalized to the peak of the underlying FTO substrate, see Fig. S1†). This displacement has been attributed to changes in the crystal structure due to the smaller size of the bromide ion compared to the iodine ion, and the fact that there is a gradual shift from the tetragonal phase of pure $MAPbI_3$ to the cubic phase of pure $MAPbBr_3$.[17,41,46] Previous reports have shown a reduction in the lattice parameters of 2–3 pm when changing between pure $MAPbI_3$ and 10% Br perovskites.[17,41,46,47] The tetragonal to cubic phase transition has been reported to occur between 13–20% bromide,[17] or at even higher bromide concentrations (>30%).[47] It has also been reported that as the amount of bromide is increased, phase segregation can occur, particularly when the film is under illumination.[16,40,41] Phase separation causes the 28.8° peak to split into two peaks, associated with iodide and bromide rich regions.[40,41] No phase separation was observed in these samples, although these films were not exposed to light before the XRD spectrum was measured. Peak splitting was observed in pure $MAPbI_3$, which is attributed to the (004) (28.11°) and (220) (28.36°) reflections of the tetragonal phase of the perovskite;[17] the peak splitting disappears with bromide addition. In order to avoid the complication of large scale phase segregation in our measurements, only bromide substitution ratios ≤7.5% were investigated.

In the next step, inverted perovskite solar cells containing different amounts of bromide were prepared and characterised. The highest reported efficiency for an inverted perovskite cell with NiO and PCBM contacts is 20.5%.[48] This efficiency was achieved with a doped hole transport layer, a modified aluminium cathode and a perovskite with a chemical composition of $MAPbI_{3-x}Cl_x$. In our lab we prepare simple inverted

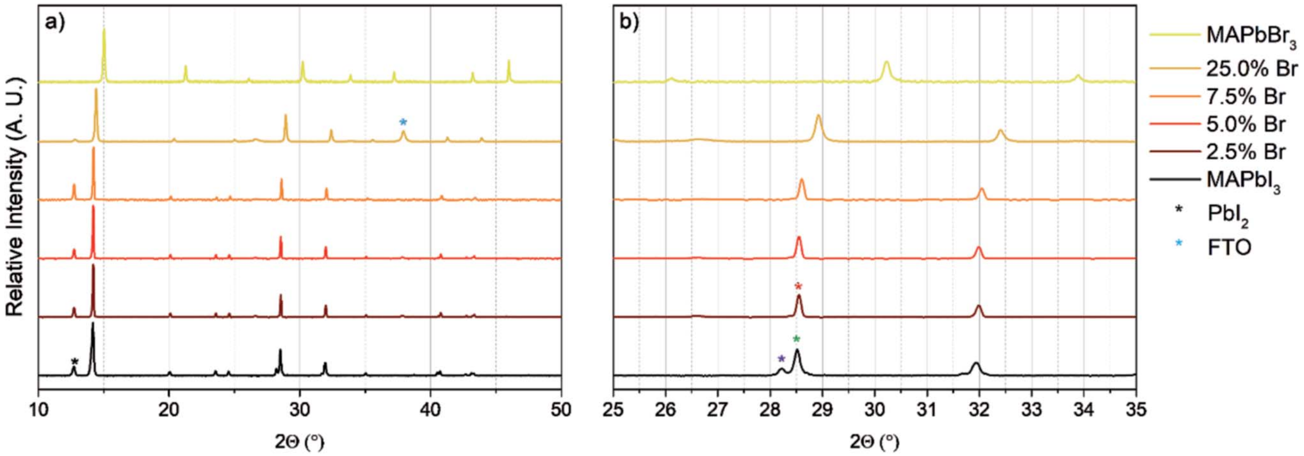

Fig. 1 XRD measurements for perovskite films with different bromide content, (a) 2θ from 10° to 65° and (b) from 25° to 35°. In (b) the main peaks for the tetragonal (004) (28.11°) (purple dot), (220) (28.36°) (green dot) and cubic phases (200) (red dot) are highlighted.

NiO cells with top efficiencies close to 15% (Fig. S2†), using a combination of anti-solvent treatments and solvent annealing. In order to make a direct comparison between cells with different bromide ratios, the cells used in this study have slightly lower efficiencies. It was much more important that direct comparisons could be made between devices with different compositions. We did not use solvent annealing, as we were concerned that it would lead to differences in crystal size between films with different bromide content. In this study cells were also prepared with an emphasis on stability and reproducibility. The cells were able to maintain a stable open circuit voltage over several hours to allow us to carry out reliable temperature dependent impedance measurements.

The influence of bromide content on perovskite solar cell performance is summarized in Fig. S3.† In Fig. S3a† the increase in V_{oc} as a function of bromide content is related with the change in the bandgap,[16–18,36,49] as shown in Fig. S4 and Table S1.† The change in current density (Fig. S3b†) is related to the absorption of the perovskite material.[17] There is a slight decrease in fill factor with increasing bromide content. All the cells showed very low hysteresis under illumination at 1 sun (Fig. S5†).

It should be noted that the performance of the devices was higher when measured from J_{sc} to V_{oc} (Fig. S5,† so called 'inverted hysteresis'). Inverted hysteresis has previously been reported for cells measured using negative preconditioning potentials.[50,51] Existing literature on inverted hysteresis refers to n–i–p perovskite cells and underlines the importance of preconditioning on the IV curve measured.[50,51] Almora *et al.* also proposed that inverted hysteresis is more likely to be observed in mixed-perovskite structures.[51] In our p–i–n cells, the preconditioning potential was always above the V_{oc} of the perovskite cell and inverted hysteresis appeared not only in mixed-halide perovskites, but also for pure $MAPbI_3$ cells (Fig. S5†). Inverted hysteresis disappears for pure $MAPbBr_3$ devices, although a direct comparison is difficult due to the lower efficiency of $MAPbBr_3$ solar cells (Fig. S3†). Our results show that inverted hysteresis is not only dependent on the preconditioning potential and the composition of the perovskite, as reported previously.[50,51]

Impedance spectroscopy (IS) was used to evaluate the influence of bromide content on ion movement. All IS was carried out at open circuit under illumination. IS is widely used to characterize PSC and the spectra vary a little depending on cell configuration and the measuring conditions used.[31,52–60] The Nyquist plots for PSC typically show 2–3 clear semi-circles, with a fourth feature that extends below the real axis at very low frequencies. In our results on both standard[31] and inverted[33] $MAPbI_3$ cells, the Nyquist plots show three semicircles when cells are measured at 25 °C under illumination (Fig. 2).We will refer to the three features as the high frequency (hf), mid-frequency (mf) and low frequency (lf) response of the device. There is still considerable debate about the interpretation of impedance spectra for PSC in the literature. There is consensus that the hf response is due to the geometric capacitance, C_{geo}, coupled to a resistance, R_{hf}.[31,53–55] R_{hf} is related to the recombination resistance, although as Ebadi *et al.* recently pointed out it could also contain a contribution from charge injection.[61] It is sometimes suggested that a transport resistance, caused by percolation of charges through the perovskite or the mesoporous oxide contact, also needs to be included.[61] However, as transfer of charge through the perovskite film is very rapid,[62] the transport resistance should be negligible in efficient cells.

In the paper by Pockett *et al.* we suggested that the mf and lf response from the cell were due to a coupled ionic-electronic response.[31] The ionic distribution inside the device is modulated by the applied voltage, this in turn modifies electron injection and recombination currents and hence causes the mf and lf impedance response. The, mf, semicircle has been associated with charge recombination,[31,55,63] although the nature of the ions causing the response in this frequency region it is still a matter of debate. The lf semicircle is associated with iodide ion modulated recombination/injection processes.[10,31,63,64] Moia *et al.* have developed a promising equivalent circuit which uses transistors to model the effect of ion modulation on electronic recombination across the

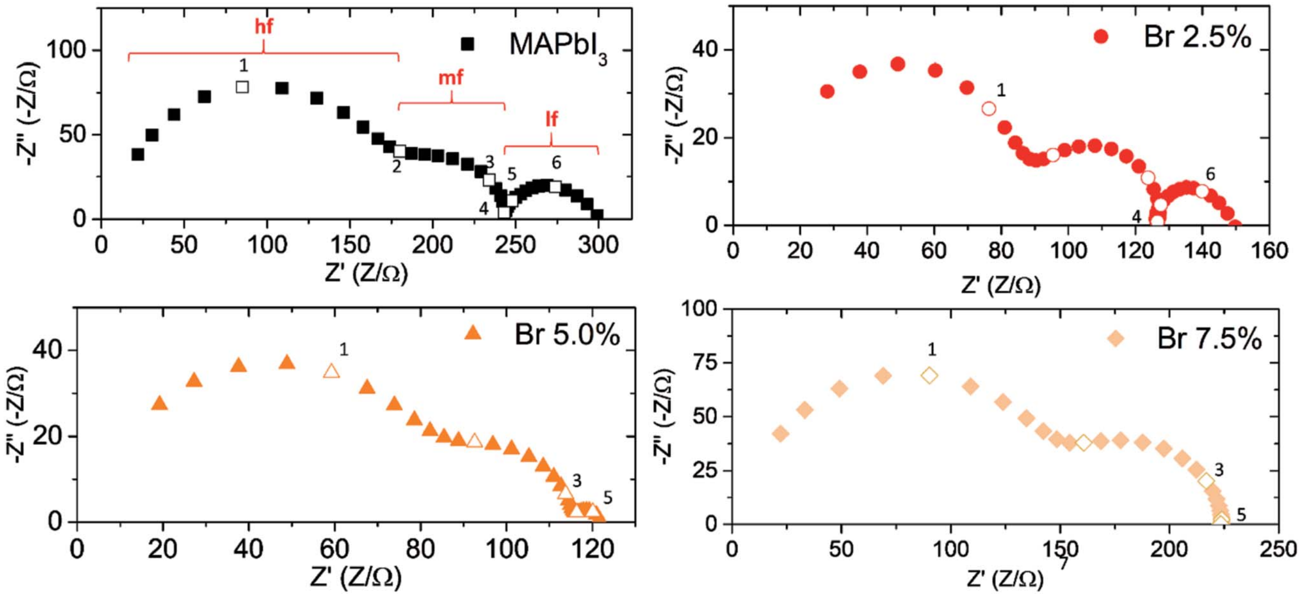

Fig. 2 Nyquist plots for perovskite solar cells as a function of the bromide content. The measurements were made at 25 °C. The high frequency (hf), mid-frequency (mf) and low frequency (lf) regions are displayed. Frequency values are highlighted in each plot: 1 = 100 kHz, 2 = 10 kHz, 3 = 1 kHz, 4 = 100 Hz, 5 = 10 Hz and 6 = 1 Hz.

interface.[65] The model can reproduce both the low frequency 'capacitive' and 'inductive' behavior inside PSC. Jacobs *et al.* use a drift diffusion model to simulate the impedance response for PSC.[66] They show that 'giant photo induced capacitances', 'induction loops' and apparent 'negative capacitances' at low frequency can all be explained by the coupling of ion migration and electronic current. The only downside of models based on transistors and semi-conductor drift diffusion models is that complex numerical solutions are required to simulate the impedance response. In our own work we also do not use an equivalent circuit to fit our data. We are taking an experimental approach – linking systematic temperature dependent IS experiments to physical processes occurring in the cell. The temperature dependent time-constant for the low frequency process can be used to extract an activation energy[31,33,64] which agrees with the majority of experimental and computational activation energies for iodide migration (0.3–0.6 eV).[11–13,29–33] We recently reported that cation substitution into MAPbI$_3$ moves the lf process to such low frequencies that it can no longer be seen in the impedance spectrum. This corresponds to a large increase in the activation energy for iodide motion inside the perovskite. Here we clearly show that the lf semi-circle can also be strongly affected by anion substitution.

The Nyquist plot for pure MAPbI$_3$ is shown in Fig. 2a. Three clear semicircles are observed, with the third semicircle appearing at frequencies lower than 100 Hz. As the amount of bromide is increased, the diameter of the low frequency semicircle decreases. For 5.0% bromide content, the semicircle is still visible although noticeably smaller than for pure MAPbI$_3$. When the bromide concentration reaches 7.5%, the low frequency semicircle has disappeared completely. The Nyquist plot for pure MAPbBr$_3$ (Fig. S6†), also shows only two clear semicircles with no trace of a third low frequency semicircle observed.

Computational studies have reported that the substitution of iodide with bromide inside the perovskite structure increases the activation energy for the migration of iodide ions.[36] The substitution of the smaller bromide ions makes the perovskite crystal more compact,[36] Ruess *et al.* suggested that this increases the interaction between the anions and MA$^+$ cations.[38] Svane *et al.* also looked at the cation–halide interaction energies in MAPbI$_3$ and MAPbBr$_3$ in detail.[67] They concluded that the hydrogen bond energy is very similar in both compounds, and that the total electrostatic energy of interaction is greater in MAPbI$_3$ than in MAPbBr$_3$. Other studies have found that bromide ions form a stronger bond with Pb^{2+} than iodide ions.[39,68]

The increase in activation energy for iodide motion in mixed halide perovskites is likely to be due to local lattice distortions. Substitution of iodide with the smaller bromide ion distorts the crystal lattice, changing ion diffusion pathways and hence increasing the activation energy for iodide motion. We recently showed that just 5% cation substitution creates enough local distortion to substantially increase the activation barrier for iodide motion.[33]

To investigate further, impedance spectra were collected at a range of different temperatures (10–40 °C). Fig. 3 shows Cole (imaginary impedance as a function of frequency) and Nyquist plots at selected temperatures for cells with 5%, 6.3% and 7.5% Br substitution. Cole plots are shown as the hf, mf and lf processes can be observed as clear "peaks" in the impedance and shifts in frequency with temperature can be more clearly observed. For perovskites with 5.0% bromide content, the low frequency peak (associated with the third lf semicircle in the

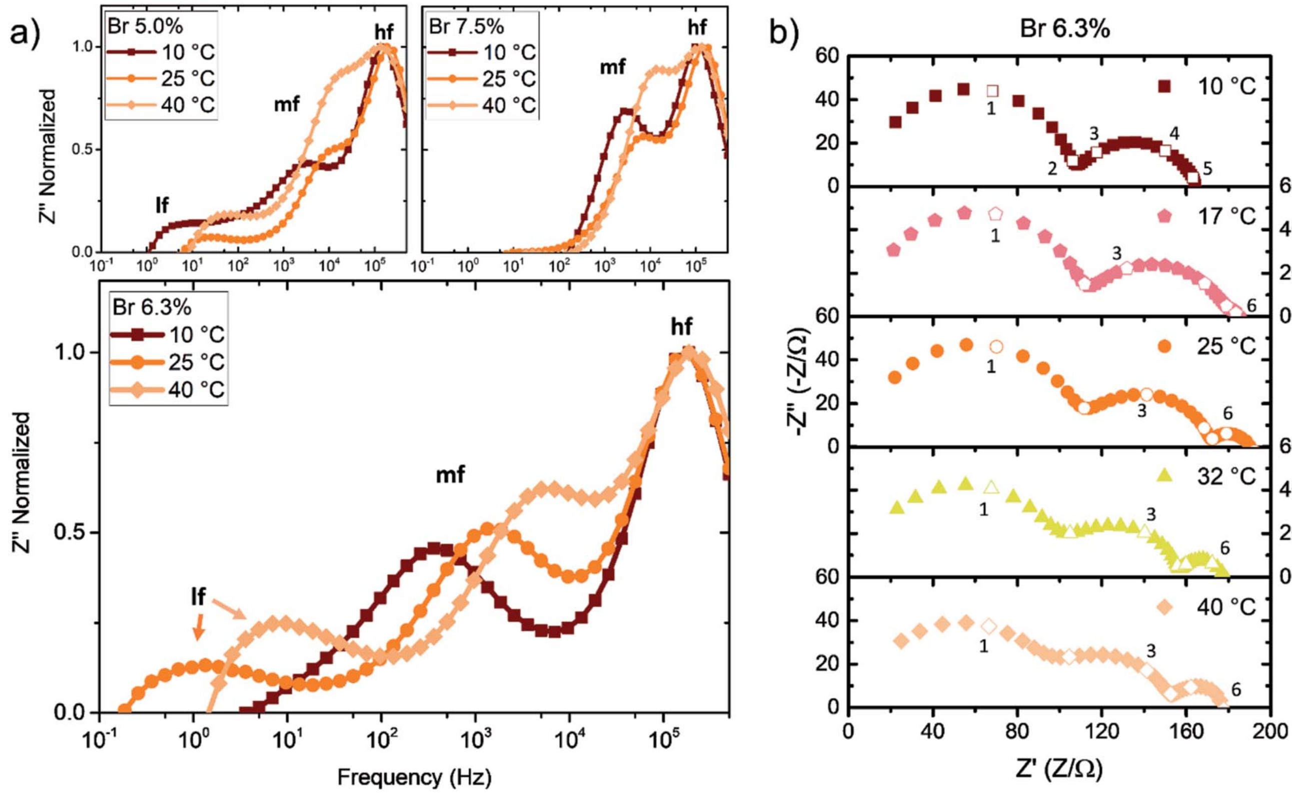

Fig. 3 (a) Cole plot of perovskite solar cells as a function of temperature and bromide concentration: 5.0%, 6.3% and 7.5% bromide content. The main peaks at different frequencies are highlighted. (b) Nyquist plots of the perovskite with 6.3% bromide concentration as a function of temperature. Frequency values are highlighted: 1 = 100 kHz, 2 = 10 kHz, 3 = 1 kHz, 4 = 100 Hz, 5 = 10 Hz and 6 = 1 Hz.

Nyquist plot) is observed at all the temperatures measured; the peak of the lf process is shifted towards higher frequencies as the temperature is increased. This is expected for a temperature activated process; the iodide motion is faster at higher temperatures. However, when the bromide concentration is increased to 7.5%, the third semicircle completely disappears, even at temperatures as high as 40 °C the lf semicircle is not visible, indicating the process that causes it has been suppressed.

An intermediate bromide concentration of 6.3% was chosen to analyze the evolution of this low frequency process. Interestingly, cells with 6.3% Br only show suppression of iodide motion at low temperature. At 10 °C only two peaks are observed with no trace of the low frequency peak. As the temperature is increased to 17 °C and beyond, the low frequency process appears. The process becomes faster as the temperature is increased and the peak in the Cole plot is observed at higher frequencies. This response shows that at 6.3% bromide concentration the iodide motion is not fast enough to affect the response at low temperatures. As the temperature is increased the amount of iodide motion increases, bringing the low frequency response into the measurement window. This effect can be fully appreciated in Fig. 3b, where the evolution of the low frequency semicircle with temperature shows the appearance of the low frequency response when going from 10 °C to 25 °C. These results suggest that there is a critical concentration of bromide over which iodide migration will be suppressed.

We used the time constants from the temperature dependent impedance measurements to obtain activation energies for the low and mid-frequency processes.[31] The results are summarized in Fig. 4. The increase in the lf activation energy with bromide concentration (red dots in Fig. 4) support the argument that iodide motion is suppressed as the bromide content is increased. This trend is consistent with the results presented in Fig. 2 and 3. Unfortunately impedance spectroscopy gives no information on the location of the ions that are causing the lf response *i.e.* whether we are measuring the influence of iodide ions moving in the bulk, along grain boundaries or at the interfaces with the hole and electron transporting contacts.

We cannot conclusively say whether the ions are modulating bulk recombination or interfacial recombination/injection. IS only provides the time scale related with the process, it does not give any information on the pathway of iodide migration/diffusion.

It is worth noting that while the high frequency process is largely independent of temperature, the mid-frequency peak shifts to higher frequencies with temperature, suggesting that this is another temperature activated process (Fig. S7†). As outlined above, the nature of the mid-frequency process is not completely understood. Our results show that it is a thermally activated process that is not strongly influenced by the bromide concentration. The mf activation energy is lowest for the pure

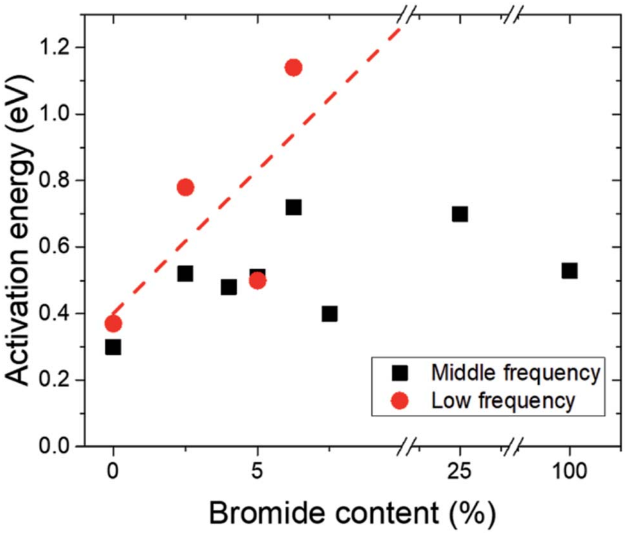

Fig. 4 Activation energy for the middle and low frequency semicircles as a function of bromide content. Dashed lines have been included as a guide for the eye. The activation energy for the low frequency process for the 6.3% bromide is highlighted as it was obtained with only three temperatures.

$MAPbI_3$ (0.3 eV) and it increases to values between 0.4–0.6 eV for mixed bromide devices where it fluctuates but does not increase sharply with Br content. The mf response has previously been shown to be particularly sensitive to illumination,[31] and has been associated with charge recombination.[31,55,63]

The mid-frequency process has an associated time constant between 0.1 and 10 ms, it is 2–3 orders of magnitude faster than the lf process. In contrast the activation energies for the mf and lf processes are very similar in $MAPbI_3$ cells. Here we measured 0.30 ± 0.08 eV for the lf and 0.37 ± 0.10 eV for the mf process in pure $MAPbI_3$ cells. It has been suggested that ion migration *via* grain boundaries should occur on faster time scales than migration through the bulk of the perovskite.[15] This leads us to think that the mf semicircle may be related to iodide migration along grain boundaries or at the interfaces with the selective contacts, whereas the lf process is caused by iodide migration in the bulk of the crystals. If this is correct, anion and cation[33] substitution suppresses bulk iodide diffusion, but does not strongly influence the motion of ions at the crystal surface. Temperature-dependent impedance measurements controlling the grain size of the perovskite may shed some light into this phenomenon but is outside the scope of this work. Equally, it would be useful to measure the temperature dependent impedance of cells where the crystallite surfaces have been passivated.[69]

It should be noted that at very low frequencies the impedance response in the Nyquist plots drops below the real axis (Fig. S8†). This response has been associated with transient injection currents,[61] however no trend in the very low frequency response of our cells was obtained as a function of bromide concentration.

Muon spin relaxation (μSR) was used as a complementary technique to further investigate iodide diffusion in $MAPb(I_{1-x}Br_x)_3$ powders. The muons used in this study stop inside the bulk of the crystals and can act as a direct probe for bulk iodide motion.[33] μSR has become a standard technique for analysis of ion migration in lithium and sodium battery materials.[70–73] Recently, we used it to study the properties of ion migration in methyl ammonium lead iodide samples as well as mixed cation samples.[33] μSR involves implanting a 100% spin polarized positive muon into a sample. The muons decay inside the sample, emitting a positron which is detected. Fluctuating electronic fields in the target material impact upon the spin of the muon, changing the decay angle of the positron and these changes can be used to gain information on the environment the muon experiences prior to decay. One possible way that the local environment of the muon can be altered is by the motion of nearby ions that have a nuclear magnetic moment. Bromide has a similar spin (3/2) and nuclear magnetic moment ($+2.12\mu_N$ for ^{79}Br and $+2.27\mu_N$ for ^{81}Br) as Li^+ (3/2 and $+3.26\mu_N$), Na^+ (3/2 and $+2.22\mu_N$) and I^- (5/2 and $+2.81\mu_N$) making it feasible to detect its migration using μSR. We recently showed that it is possible to detect iodide diffusion in $MAPbI_3$ above 350 K.[33]

Here we carried out μSR on pure $MAPbBr_3$ and on $MAPb(I_{0.83}Br_{0.17})_3$. Powder samples of $MAPbBr_3$ and $MAPb(I_{0.83}Br_{0.17})_3$ were prepared and characterized with pXRD (Fig. S9†). For the study of $MAPBr_3$, measurements were taken at regular temperature intervals between 50 and 400 K with four different longitudinal field measurements (0, 5, 10 and 20 Gauss) taken at each temperature. The resulting data was fit using a dynamic Gaussian Kubo Toyabe function multiplied by an exponential relaxation (eqn (1)):[72]

$$A_0 P_{LF} = A_{KT} G^{DGKT}(\Delta, \nu, t, H_{LF}) \exp(-\lambda t) + A_{BG} \tag{1}$$

The terms A_0, A_{BG}, A_{KT} refer to the initial, background and sample asymmetry, respectively. P_{LF} is the polarization in a longitudinal field, G^{DGKT} refers to a dynamic Gaussian Kubo Toyabe (KT) distribution function, Δ is the local field formed by nuclear magnetic moments at the muon implantation site, ν is the dynamic fluctuation rate of the local field, t is time and H_{LF} is the applied longitudinal magnetic field. Finally, $\exp(-\lambda t)$ is used to model the depolarization of muons caused by electronic moments, the rate of fluctuation is so rapid that it can be modelled by a simple exponential function with λ as the rate of relaxation. A small non-zero value of λ (less than 0.02 MHz) was found to be necessary to consistently describe the data across the full temperature range and can be attributed to a slight difference between the field distribution in the samples and the Gaussian approximation of the G^{DGKT} function. An example of raw muon data for $MAPbBr_3$ at 100 K is shown in Fig. S10.†

The dynamic fluctuation rate, ν, can be linked to ions moving in the perovskite powders. By fitting the asymmetry data across the full temperature range, it is possible to obtain values for ν with respect to temperature (Fig. 5). We have presented the data for $MAPbI_3$ previously, but it is reproduced here for clarity. In $MAPbI_3$ ν first increases between about 100 K and 150 K. This increase in fluctuation rate at low temperatures is caused by the muons interacting with the MA cations which can change orientation inside the lattice (they are not diffusing at these

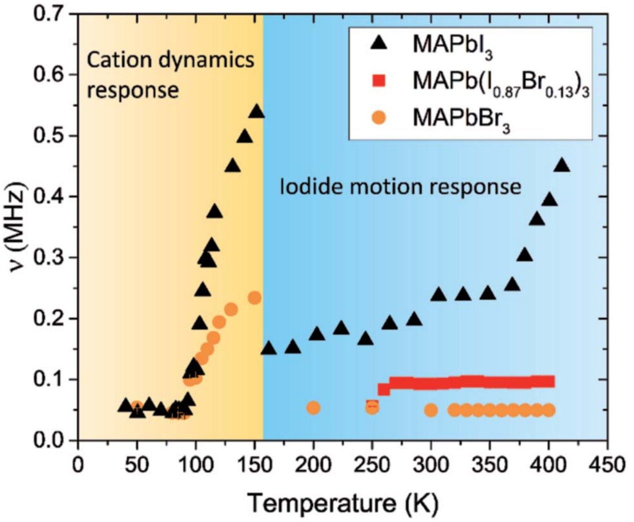

Fig. 5 Temperature dependence of ν for MAPbI$_3$, MAPbBr$_3$ and MAPb(I$_{0.83}$Br$_{0.17}$)$_3$. The regions where the cation and anion response are expected are highlighted. The results of MAPbI$_3$ have been adapted with permission.[33]

temperatures).[74] Above 150 K, cation tumbling becomes too fast to be measured by μSR. At temperatures greater than 250 K in MAPbI$_3$ there is a second increase in ν which is due to the motion of iodide ions. ν increases steeply after 350 K as iodide diffusion strongly influences the measured response. By fitting the increase in ν as a function of temperature, an activation energy for iodide motion can be obtained.

The ν data for MAPbBr$_3$ shows only one increase in fluctuation between 100 K and 150 K, again this is where the cations would be expected to have enough energy to reorient inside the lattice.

After 150 K the fluctuation rate decreases back down to 0.05 MHz where it remains flat for the rest of the temperature range. The results of the MAPBr$_3$ study show that cation dynamics are still prevalent at low temperature and the process has an E_a of 0.026 eV (Fig. S11†). This compared to an activation energy of 0.072 eV for the cations in MAPbI$_3$.[33] The complete absence of any high temperature increase in fluctuation rate shows that it was not possible to detect bromide ions moving in the same way that we were able to detect iodide motion in pure MAPbI$_3$.[33]

The mixed halide perovskite MAPb(I$_{0.83}$Br$_{0.17}$)$_3$ was studied between 250 and 400 K as this is the temperature range where iodide motion is observed in pure MAPbI$_3$ (Fig. 5).[33] The data was fit using the same parameterization as the MAPbBr$_3$ study and the resulting temperature dependence of ν is shown in Fig. 5. The fluctuation rate was not affected by the increase in temperature. This indicates that bulk iodide diffusion was not detectable in the mixed halide sample. This agrees with the impedance results which show bromide inhibiting iodide diffusion.

In the final part of this study, the effect of anion mixing on *J–V* curve hysteresis is investigated. Hysteresis in perovskite cells has been associated with ion migration and charge redistribution in the perovskite crystal, and it has also been used as an indirect way to study ion migration in perovskite solar cells.[12,13,26]

Several groups have investigated the dependence of hysteresis on scan rate and related the response to the timescale of the redistribution of charge as the applied external potential changes.[11,26,75] By measuring hysteresis across a broad range of scan rates the timescale at which maximum hysteresis is observed can be reported.[13,75,76]

Our impedance and μSR results suggest that bromide content strongly influences iodide motion in the perovskite structure. We therefore expected bromide content to influence the scan rate at which peak hysteresis is observed. We measured *J–V* curves with different scan rates (Fig. S12–S16†) and obtained the degree of hysteresis as a function of scan rate and bromide concentration according to the procedure presented in the ESI (eqn S1†). The results are summarized in Fig. 6. The PSC showed inverted hysteresis at the majority of scan rates investigated. It should be noted that for these measurements the cells were measured at fixed temperature under blue LED illumination. The degree of hysteresis was much higher under blue light than under 1 sun illumination (Fig. S5†). The difference in the degree of hysteresis may be related with differences in the penetration depth of the light, and as a consequence the generation profile of carriers inside the perovskite, as was proposed by Contreras-Bernal *et al.*[52] This could be related to

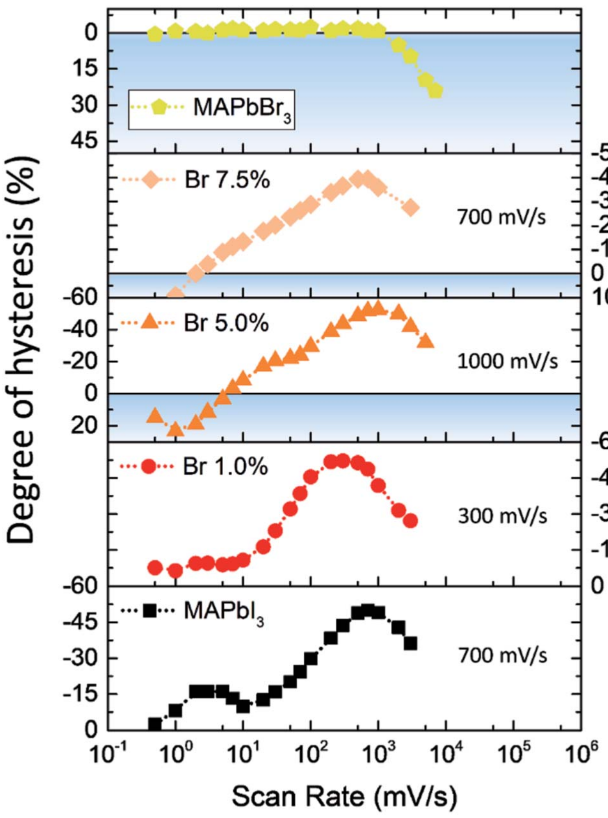

Fig. 6 Degree of hysteresis as a function of scan rate and bromide content in perovskite solar cells. The scan rate at which the peak of hysteresis is observed for each concentration is presented. The blue shade represents the region where normal hysteresis is present.

the experimental finding that hysteresis is closely related to the nature of the selective contacts.[28,42–44]

Fig. 6 shows that, surprisingly, the scan rate at which the maximum hysteresis is observed does not change noticeably with small additions of bromide. However, there are clear changes for pure bromide devices which show no hysteresis up to 1000 mV s^{-1}.

It has already been reported that "hysteresis-free" devices, such as inverted perovskite cells are simply devices where the timescale of the process responsible of the hysteretic behavior is not observable under the measurement conditions presented (*e.g.* hysteresis is low at 100–200 mV s^{-1}, but not at other scan rates).[13,77] Although the inverted perovskite cells measured here show very low hysteresis under 1 sun illumination and a scan rate of 100 mV s^{-1} (Fig. S5†), our results show that under blue light the hysteresis increases at faster scan rates (Fig. 6).

The peak hysteresis for our inverted cell is remarkably similar to peak hysteresis reported by Levine *et al.* for pure $MAPbI_3$.[13] They found that peak hysteresis for inverted cells appeared at higher scan rates than for traditional n–i–p cells (between 300–1500 mV s^{-1}), the shift was attributed to differences between the selective contacts. Levine *et al.*[13] and Bryant *et al.*[77] also found that lowering the temperature, and hence slowing ion motion, in inverted perovskite solar cells increases the degree of hysteresis.

The results presented in Fig. 6 highlight the differences between hysteresis and impedance measurements (Fig. 2 and 3). A direct relationship between low frequency impedance response and hysteresis has been recently proposed by Ebadi *et al.*[61] Their results showed that devices with a negative capacitive response at low frequencies were more likely to show hysteretic behavior with a stronger dependence on scan rate. However, our results show that changes in the impedance response at low frequencies are not necessarily observed in hysteresis measurements, and *vice versa*. Although both, low-frequency impedance[10,31,33,63,64] and hysteresis[12,13,26] measurements, are usually related with ion migration, these measurements are fundamentally different.

For the impedance measurements we apply a small potential perturbation (10 mV) to ensure linearity on the system;[31,78] for hysteresis measurements the changes in potential are larger (from V_{oc} to J_{sc} and *vice versa*) and we are no longer under steady state conditions. Care needs to be taken when comparing steady state and dynamic measurements. However, it is interesting to roughly compare 'timescales'. The impedance results for the low frequency semicircle appear at frequencies below 100 Hz. If the amplitude of the small perturbation is 10 mV, it means that at 1 Hz there will be a change of 20 mV, *e.g.*, when the measurement frequency is 1 Hz, we have a potential change of 20 mV s^{-1}. At 100 Hz the change in potential will be 2000 mV s^{-1}, which means that the low frequency semicircle is related with changes in potential of approximately 2000 mV s^{-1} and lower, which will include most of the scan rates employed for the hysteresis measurements in this study. However, with impedance measurements we observe a clear change with the inclusion of bromide, while for hysteresis measurements there are only small differences. In some of the hysteresis measurements it is possible to observe two different peaks in the degree of hysteresis, possibly related with two processes with different time constants, as previously reported by Bryant *et al.*[77]

All our evidence supports the argument that the low frequency process in impedance is related to ion motion, as previously reported in the literature.[10,31,63,64] We go a step further and relate this process with iodide migration, a result which is supported by muon spectroscopy. Bromide substitution strongly affects both the impedance measurements and the muon spectroscopy; it does not affect hysteresis. There is considerable evidence to suggest that ion migration causes hysteresis. However, the nature of the hysteresis process is clearly more complicated.

There are several possible reasons for the differences between IS and hysteresis measurements. As mentioned above, we believe that faster ion migration at grain boundaries/interfaces can still occur in all the devices and the easy motion of surface ions in response to the applied voltage could explain IV hysteresis. IV curve hysteresis has also been more closely linked to the nature of the hole and electron selective contacts used in the cells, and it is possible that it is the interaction of surface ions with the contact that is causing hysteresis.

Conclusions

Our results show that by incorporating small amounts of bromide into the perovskite structure, the low frequency impedance response is strongly affected. We attribute this change to a suppression of bulk iodide motion, probably due to local distortions/contractions in the crystal structure with the introduction of small Br ions as increasing Br substitution increases the activation energy for iodide motion. We show there is a critical bromide concentration after which the iodide migration can no longer be observed. Muon spin relaxation measurements support the conclusion that the incorporation of bromide in the perovskite inhibits bulk iodide motion. In contrast, hysteresis measurements show that the scan rate at which the hysteresis is largest is not related to the amount of bromide inside the perovskite. Although both are influenced by ion motion, hysteresis and impedance measurements appear to provide different information about the perovskite device. By increasing understanding of two of the most common techniques used to measure perovskite solar cells, IV curves measurements and impedance spectroscopy, we are moving one step closer to understanding the fundamental processes in perovskite devices.

Conflicts of interest

There are no conflicts to declare.

Acknowledgements

Rodrigo García-Rodríguez gratefully acknowledges CONACYT for support through a postdoctoral scholarship. Sam Pering was supported by the University of Bath, Dominic Ferdani was supported by the Centre for Doctoral Training in Sustainable Chemical Technologies (studentship under grant EP/L016354/1). We thank the STFC for the allocated muon beamtime. Muon data is available electronically at the following site https://doi.org/10.5286/ISIS.E.RB1810384. Additional data that support the findings of this study are available from the corresponding author, PJC, upon reasonable request

Notes and references

1 A. Kojima, K. Teshima, Y. Shirai and T. Miyasaka, *J. Am. Chem. Soc.*, 2009, **131**, 6050–6051.

2 M. A. Green, Y. Hishikawa, E. D. Dunlop, D. H. Levi, H.-E. Jochen, Y. Masahiro and A. W. Y. Ho-Baillie, *Prog. Photovolt. Res. Appl.*, 2019, **27**, 3–12.

3 W. S. Yang, J. H. Noh, J. J. Nam, Y. C. Kim, S. Ryu, J. Seo and S. Il Seok, *Science*, 2015, **348**, 1234–1237.

4 M. A. Green, E. D. Dunlop, D. H. Levi, J. Hohl-Ebinger, M. Yoshita and A. W. Y. Ho-Baillie, *Prog. Photovolt. Res. Appl.*, 2019, **27**, 565–575.

5 J. Ramanujam and U. P. Singh, *Energy Environ. Sci.*, 2017, **10**, 1306–1319.

6 T. D. Lee and A. U. Ebong, *Renewable Sustainable Energy Rev.*, 2017, **70**, 1286–1297.

7 L. Lu, T. Zheng, Q. Wu, A. M. Schneider, D. Zhao and L. Yu, *Chem. Rev.*, 2015, **115**, 12666–12731.

8 A. Hagfeldt, G. Boschloo, L. Sun, L. Kloo and H. Pettersson, *Chem. Rev.*, 2010, **110**, 6595–6663.

9 B. E. Hardin, J. Snaith and M. D. Mcgehee, *Nat. Photonics*, 2012, **6**, 162–169.

10 L. Contreras, J. Idígoras, A. Todinova, M. Salado, S. Kazim, S. Ahmad and J. A. Anta, *Phys. Chem. Chem. Phys.*, 2016, **18**, 31033–31042.

11 C. Eames, J. M. Frost, P. R. F. Barnes, B. C. O'Regan, A. Walsh and M. S. Islam, *Nat. Commun.*, 2015, **6**, 1–8.

12 M. L. Petrus, J. Schlipf, C. Li, T. P. Gujar, N. Giesbrecht, P. Müller-Buschbaum, M. Thelakkat, T. Bein, S. Hüttner and P. Docampo, *Adv. Energy Mater.*, 2017, **7**, 1700264.

13 I. Levine, P. K. Nayak, J. T. W. Wang, N. Sakai, S. Van Reenen, T. M. Brenner, S. Mukhopadhyay, H. J. Snaith, G. Hodes and D. Cahen, *J. Phys. Chem. C*, 2016, **120**, 16399–16411.

14 E. Mosconi, D. Meggiolaro, H. J. Snaith, S. D. Stranks and F. De Angelis, *Energy Environ. Sci.*, 2016, **9**, 3180–3187.

15 Y. Yuan and J. Huang, *Acc. Chem. Res.*, 2016, **49**, 286–293.

16 A. F. Gualdrón-Reyes, S. J. Yoon, E. M. Barea, S. Agouram, V. Muñoz-Sanjosé, Á. M. Meléndez, M. E. Niño-Gómez and I. Mora-Seró, *ACS Energy Lett.*, 2018, 54–62.

17 J. H. Noh, S. H. Im, J. H. Heo, T. N. Mandal and S. Il Seok, *Nano Lett.*, 2013, **13**, 1764–1769.

18 N. Pellet, J. Teuscher, J. Maier and M. Grätzel, *Chem. Mater.*, 2015, **27**, 2181–2188.

19 O. A. Jaramillo-Quintero, R. S. Sánchez, M. Rincón and I. Mora-Sero, *J. Phys. Chem. Lett.*, 2015, **6**, 1883–1890.

20 B. Zhao, S. Bai, V. Kim, R. Lamboll, R. Shivanna, F. Auras, J. M. Richter, L. Yang, L. Dai, M. Alsari, X. J. She, L. Liang, J. Zhang, S. Lilliu, P. Gao, H. J. Snaith, J. Wang, N. C. Greenham, R. H. Friend and D. Di, *Nat. Photonics*, 2018, **12**, 783–789.

21 K. A. Bush, A. F. Palmstrom, Z. J. Yu, M. Boccard, R. Cheacharoen, J. P. Mailoa, D. P. McMeekin, R. L. Z. Hoye, C. D. Bailie, T. Leijtens, I. M. Peters, M. C. Minichetti, N. Rolston, R. Prasanna, S. Sofia, D. Harwood, W. Ma, F. Moghadam, H. J. Snaith, T. Buonassisi, Z. C. Holman, S. F. Bent and M. D. McGehee, *Nat. Energy*, 2017, **2**, 1–7.

22 E. E. Giles, L. Tomas, B. A. Kevin, P. Rohit, G. Thomas, W. Jacob Tse-Wei, M. P. David, V. George, M. L. Rebecca, M. Richard, P. Axel, S. J. Daniel, B. A. Rebecca, P. B. Jay, P. S. Elizabeth, S. J. Rebecca, M. Wen, M. Farhad, C. Bert, B. Aslihan, B. Hans-Gerd, B. Stacey, G. Feliciano, H. M. Laura, J. B. Michael, M. D. Michael and S. J. Henry, *Science*, 2016, **354**, 861.

23 H. S. Kim, J. Y. Seo and N. G. Park, *ChemSusChem*, 2016, **9**, 2528–2540.

24 S. Yang, W. Fu, Z. Zhang, H. Chen and C. Z. Li, *J. Mater. Chem. A*, 2017, **5**, 11462–11482.

25 J. Berry, T. Buonassisi, D. A. Egger, G. Hodes, L. Kronik, Y. L. Loo, I. Lubomirsky, S. R. Marder, Y. Mastai, J. S. Miller, D. B. Mitzi, Y. Paz, A. M. Rappe, I. Riess, B. Rybtchinski, O. Stafsudd, V. Stevanovic, M. F. Toney, D. Zitoun, A. Kahn, D. Ginley and D. Cahen, *Adv. Mater.*, 2015, **27**, 5102–5112.

26 W. Tress, N. Marinova, T. Moehl, S. M. Zakeeruddin, M. K. Nazeeruddin and M. Grätzel, *Energy Environ. Sci.*, 2015, **8**, 995–1004.

27 C. Eames, J. M. Frost, P. R. F. Barnes, B. C. O'Regan, A. Walsh and M. S. Islam, *Nat. Commun.*, 2015, **6**, 1–8.

28 M. De Bastiani, G. Dell'Erba, M. Gandini, V. D'Innocenzo, S. Neutzner, A. R. S. Kandada, G. Grancini, M. Binda, M. Prato, J. M. Ball, M. Caironi and A. Petrozza, *Adv. Energy Mater.*, 2016, **6**, 1–9.

29 J. M. Azpiroz, E. Mosconi, J. Bisquert and F. De Angelis, *Energy Environ. Sci.*, 2015, **8**, 2118–2127.

30 Y. Yuan, Q. Wang, Y. Shao, H. Lu, T. Li, A. Gruverman and J. Huang, *Adv. Energy Mater.*, 2016, **6**, 1501803.

31 A. Pockett, G. Eperon, N. Sakai, H. Snaith, L. M. Peter and P. J. Cameron, *Phys. Chem. Chem. Phys.*, 2017, **19**, 5959–5970.

32 S. Meloni, T. Moehl, W. Tress, M. Franckevicius, M. Saliba, Y. H. Lee, P. Gao, M. K. Nazeeruddin, S. M. Zakeeruddin, U. Rothlisberger and M. Graetzel, *Nat. Commun.*, 2016, **7**, 10334.

33 D. Ferdani, S. Pering, D. Ghosh, P. Kubiak, A. Walker, S. E. Lewis, A. L. Johnson, P. J. Baker, S. Islam and P. J. Cameron, *Energy Environ. Sci.*, 2019, **12**, 2264–2272.

34 Y. Yuan, J. Chae, Y. Shao, Q. Wang, Z. Xiao, A. Centrone and J. Huang, *Adv. Energy Mater.*, 2015, **5**, 1500615.

35 Z. Xiao, Y. Yuan, Y. Shao, Q. Wang, Q. Dong, C. Bi, P. Sharma, A. Gruverman and J. Huang, *Nat. Mater.*, 2015, **14**, 193–198.

36 C. Lin, S. Li, W. Zhang, C. Shao and Z. Yang, *ACS Appl. Energy Mater.*, 2018, **1**, 1374–1380.

37 J. H. Noh, S. H. Im, J. H. Heo, T. N. Mandal and S. Il Seok, *Nano Lett.*, 2013, **13**, 1764–1769.

38 R. Ruess, F. Benfer, F. Böcher, M. Stumpp and D. Schlettwein, *ChemPhysChem*, 2016, **17**, 1505–1511.

39 S. J. Yoon, M. Kuno and P. V. Kamat, *ACS Energy Lett.*, 2017, **2**, 1507–1514.

40 M. Hu, C. Bi, Y. Yuan, Y. Bai and J. Huang, *Adv. Sci.*, 2015, **3**, 6–11.

41 E. T. Hoke, D. J. Slotcavage, E. R. Dohner, A. R. Bowring, H. I. Karunadasa and M. D. McGehee, *Chem. Sci.*, 2015, **6**, 613–617.

42 H.-S. Kim, I.-H. Jang, N. Ahn, M. Choi, A. Guerrero, J. Bisquert and N.-G. Park, *J. Phys. Chem. Lett.*, 2015, **6**, 4633–4639.

43 J. Xu, A. Buin, A. H. Ip, W. Li, O. Voznyy, R. Comin, M. Yuan, S. Jeon, Z. Ning, J. J. McDowell, P. Kanjanaboos, J. P. Sun, X. Lan, L. N. Quan, D. H. Kim, I. G. Hill, P. Maksymovych and E. H. Sargent, *Nat. Commun.*, 2015, **6**, 1–8.

44 Y. Shao, Z. Xiao, C. Bi, Y. Yuan and J. Huang, *Nat. Commun.*, 2014, **5**, 5784.

45 J. I. Pankove, *Optical Processes in Semiconductors*, Dover, New Jersey, 1971.

46 R. G. Niemann, A. G. Kontos, D. Palles, E. I. Kamitsos, A. Kaltzoglou, F. Brivio, P. Falaras and P. J. Cameron, *J. Phys. Chem. C*, 2016, **120**, 2509–2519.

47 B. W. Park, B. Philippe, S. M. Jain, X. Zhang, T. Edvinsson, H. Rensmo, B. Zietz and G. Boschloo, *J. Mater. Chem. A*, 2015, **3**, 21760–21771.

48 S. Yue, K. Liu, R. Xu, M. Li, M. Azam, K. Ren, J. Liu, Y. Sun, Z. Wang, D. Cao, X. Yan, S. Qu, Y. Lei and Z. Wang, *Energy Environ. Sci.*, 2017, **10**, 2570–2578.

49 R. G. Niemann, A. G. Kontos, D. Palles, E. I. Kamitsos, A. Kaltzoglou, F. Brivio, P. Falaras and P. J. Cameron, *J. Phys. Chem. C*, 2016, **120**, 2509–2519.

50 G. A. Nemnes, C. Besleaga, V. Stancu, D. E. Dogaru, L. N. Leonat, L. Pintilie, K. Torfason, M. Ilkov, A. Manolescu and I. Pintilie, *J. Phys. Chem. C*, 2017, **121**, 11207–11214.

51 O. Almora, P. Lopez-Varo, K. T. Cho, S. Aghazada, W. Meng, Y. Hou, C. Echeverría-Arrondo, I. Zimmermann, G. J. Matt, J. A. Jiménez-Tejada, C. J. Brabec, M. K. Nazeeruddin and G. Garcia-Belmonte, *Sol. Energy Mater. Sol. Cells*, 2019, **195**, 291–298.

52 L. Contreras-Bernal, M. Salado, A. Todinova, L. Calio, S. Ahmad, J. Idígoras and J. A. Anta, *J. Phys. Chem. C*, 2017, **121**, 9705–9713.

53 E. Guillén, F. J. Ramos, J. A. Anta and S. Ahmad, *J. Phys. Chem. C*, 2014, **118**, 22913–22922.

54 L. Contreras-Bernal, C. Aranda, M. Valles-Pelarda, T. T. Ngo, S. Ramos-Terrón, J. J. Gallardo, J. Navas, A. Guerrero, I. Mora-Sero, J. Idigoras and J. A. Anta, *J. Phys. Chem. C*, 2018, **122**, 5341–5348.

55 A. Pockett, G. E. Eperon, T. Peltola, H. J. Snaith, A. Walker, L. M. Peter and P. J. Cameron, *J. Phys. Chem. C*, 2015, **119**, 3456–3465.

56 B. Suarez, V. Gonzalez-Pedro, T. S. Ripolles, R. S. Sanchez, L. Otero and I. Mora-Sero, *J. Phys. Chem. Lett.*, 2014, **5**, 1628–1635.

57 K. Cao, H. Li, S. S. Liu, J. Cui, Y. Shen and M. Wang, *Nanoscale*, 2016, **8**, 8839–8846.

58 I. Zarazua, G. Han, P. P. Boix, S. Mhaisalkar, F. Fabregat-Santiago, I. Mora-Seró, J. Bisquert and G. Garcia-Belmonte, *J. Phys. Chem. Lett.*, 2016, **7**, 5105–5113.

59 I. Zarazúa, S. Sidhik, T. Lopéz-Luke, D. Esparza, E. De La Rosa, J. Reyes-Gomez, I. Mora-Seró and G. Garcia-Belmonte, *J. Phys. Chem. Lett.*, 2017, **8**, 6073–6079.

60 A. R. Pascoe, N. W. Duffy, A. D. Scully, F. Huang and Y. B. Cheng, *J. Phys. Chem. C*, 2015, **119**, 4444–4453.

61 F. Ebadi, N. Taghavinia, R. Mohammadpour, A. Hagfeldt and W. Tress, *Nat. Commun.*, 2019, **10**, 1574.

62 S. D. Stranks, G. E. Eperon, G. Grancini, C. Menelaou, M. J. P. Alcocer, T. Leijtens, L. M. Herz, A. Petrozza and H. J. Snaith, *Science*, 2013, **342**, 341–344.

63 A. Guerrero, G. Garcia-Belmonte, I. Mora-Sero, J. Bisquert, Y. S. Kang, T. J. Jacobsson, J. P. Correa-Baena and A. Hagfeldt, *J. Phys. Chem. C*, 2016, **120**, 8023–8032.

64 M. Bag, L. A. Renna, R. Y. Adhikari, S. Karak, F. Liu, P. M. Lahti, T. P. Russell, M. T. Tuominen and D. Venkataraman, *J. Am. Chem. Soc.*, 2015, **137**, 13130–13137.

65 D. Moia, I. Gelmetti, P. Calado, W. Fisher, M. Stringer, O. Game, Y. Hu, P. Docampo, D. Lidzey, E. Palomares, J. Nelson and P. R. F. F. Barnes, *Energy Environ. Sci.*, 2019, **12**, 1296–1308.

66 D. A. Jacobs, H. Shen, F. Pfeffer, J. Peng, T. P. White, F. J. Beck and K. R. Catchpole, *J. Appl. Phys.*, 2018, **124**, 225702.

67 K. L. Svane, A. C. Forse, C. P. Grey, G. Kieslich, A. K. Cheetham, A. Walsh and K. T. Butler, *J. Phys. Chem. Lett.*, 2017, **8**, 6154–6159.

68 S. J. Yoon, K. G. Stamplecoskie and P. V. Kamat, *J. Phys. Chem. Lett.*, 2016, **7**, 1368–1373.

69 M. Abdi-Jalebi, Z. Andaji-Garmaroudi, S. Cacovich, C. Stavrakas, B. Philippe, J. M. Richter, M. Alsari, E. P. Booker, E. M. Hutter, A. J. Pearson, S. Lilliu, T. J. Savenije, H. Rensmo, G. Divitini, C. Ducati, R. H. Friend and S. D. Stranks, *Nature*, 2018, **555**, 497–501.

70 J. Sugiyama, K. Mukai, H. Nozaki, M. Harada, K. Kamazawa, Yutakaikedo, M. Månsson, O. Ofer, E. J. Ansaldo, J. H. Brewer, K. H. Chow, Isaowatanabe, Y. Miyake and T. Ohzuku, *Phys. Procedia*, 2012, **30**, 105–108.

71 M. Månsson and J. Sugiyama, *Phys. Scr.*, 2013, **88**, 068509.

72 J. Sugiyama, K. Mukai, Y. Ikedo, H. Nozaki, M. Månsson and I. Watanabe, *Phys. Rev. Lett.*, 2009, **103**, 147601.

73 T. E. Ashton, J. V. Laveda, D. A. MacLaren, P. J. Baker, A. Porch, M. O. Jones and S. A. Corr, *J. Mater. Chem. A*, 2014, **2**, 6238.

74 D. Ghosh, P. Walsh Atkins, M. S. Islam, A. B. Walker and C. Eames, *ACS Energy Lett.*, 2017, **2**, 2424–2429.

75 A. Pockett and M. J. Carnie, *ACS Energy Lett.*, 2017, **2**, 1683–1689.

76 S. Van Reenen, M. Kemerink and H. J. Snaith, *J. Phys. Chem. Lett.*, 2015, **6**, 3808–3814.

77 D. Bryant, S. Wheeler, B. C. O'Regan, T. Watson, P. R. F. Barnes, D. Worsley and J. Durrant, *J. Phys. Chem. Lett.*, 2015, **6**, 3190–3194.

78 D. Pitarch-Tena, T. T. Ngo, M. Vallés-Pelarda, T. Pauporté and I. Mora-Seró, *ACS Energy Lett.*, 2018, **3**, 1044–1048.